

# Theoretical investigation of patterned two-dimensional semiconductors for tailored light–matter interactions

Christian Nicolaisen Hansen \*, Line Jelver , and Christos Tserkezis †

*POLIMA—Center for Polariton-driven Light-Matter Interactions,  
University of Southern Denmark, 5230 Odense M, Denmark*

(Dated: December 16, 2025)

We introduce theoretical methods for describing the optical response of two-dimensional (2D) materials patterned at the nanoscale into both arrays of ribbons along a planar surface and spherical particles. Fourier-Floquet decompositions of the electromagnetic fields are used in order to obtain the reflectance, transmittance and absorbance of the nanoribbon array. The spherical particles consist of a vacuum or dielectric core, coated by single 2D material layers. A Mie theory, with boundary conditions modified to accommodate a 2D material at the interface, is applied to theoretically examine these spherical particles. As examples of 2D materials, we consider the excitonic response of hexagonal boron nitride in the ultraviolet, and of the transition-metal dichalcogenide WS<sub>2</sub> in the visible. The most important steps and equations for implementing the various methods are provided as a means to an easy introduction to the theory of patterned 2D materials. This renders the article a toolset for investigating the patterning of any 2D material with the intention to tune their optical response and/or introduce hybridization schemes with their excitons. The methods are not restricted to exciton polaritons in 2D semiconductors, but can be applied, by simple replacement of the optical conductivity, to 2D materials exhibiting any polaritonic response.

## I. INTRODUCTION

Two-dimensional (2D) materials have attracted much attention within nanophotonics since the emergence of graphene [1–3]. These layered materials, where each of the atomically-thin layers are connected by van der Waals forces, have exhibited a wide diversity of new electronic and photonic phenomena [4–6]. For 2D materials exhibiting a band gap, external electromagnetic (EM) radiation can excite electrons from the valence band to the conduction band, leaving a hole in the conduction band. The generated electron–hole pairs form charge-neutral quasiparticles known as excitons. Of special interest for this tutorial are the EM modes confined to the plane of the 2D material as the excitons couple to the external radiation. These modes are known as exciton polaritons, being one characteristic example among the wide range of possible polaritons [7]. Here, inspired by the case of graphene, we explore how to tune their optical response by patterning the 2D material into nanoscale geometries. We explore the theory of such patterning in two different situations: hexagonal boron nitride (hBN), with a large band gap and ultraviolet (UV) activity, and tungsten disulfide (WS<sub>2</sub>), being a transition metal dichalcogenide (TMD) [8, 9] with a large excitonic response in the visible regime.

The former material, hBN, has shown promise for the detection of biomolecules known as cyclic  $\beta$ -helical peptides [10–12]. These molecules are important in the biophysics of the body and exhibit intense absorption at wavelengths between 200 and 240 nm. By using hBN as a material with a spectral response in the same UV range,

one is able to investigate their chirality, namely the property of the molecule not being superposable onto its own mirror image. The atomically-flat surface of hBN, and its ability to support exciton polaritons in the UV, could therefore allow for the fabrication of optical sensors to detect these cyclic  $\beta$ -helical peptides. On the other hand, the optical response, of TMDs in general, and WS<sub>2</sub> in particular, in the visible regime, is of special interest for applications in optoelectronic devices. Compared to bulk semiconductors, these 2D materials have potential as ultrathin, flexible, and nearly transparent optoelectronic devices at low cost [13–18].

Within nanophotonics, both hBN and WS<sub>2</sub> have been studied extensively due to their polaritonic response, with examples being phonon polaritons in the infrared (IR) for hBN [19, 20] and valley polaritons in TMDs [21]. The control of such polaritons has led to a multitude of applications, for instance within polaritonic transistors and lasing [22, 23], while at the same time providing a fruitful platform for studies of fundamental physics, e.g. in the context of Bose-Einstein condensation, polariton blockade, polaritonic simulators and optical nonlinearities [24].

The paper is structured as follows; section II introduces the methods for modeling the optical conductivity of both hBN and WS<sub>2</sub>. The optical conductivity will, for a given geometry, be implemented in the EM boundary conditions to introduce the 2D material into the system. Section III looks into methods for patterning 2D materials into an array of ribbons placed on a dielectric substrate. Finally, section IV considers the patterning of the 2D material into spherical geometries; hollow shells and coatings around cores of a dielectric material. These geometries are modeled using methods that have been developed for single-layer graphene. This paper adapts these methods for 2D semiconductors in a tutorial style,

\* [nicolaisen@mci.sdu.dk](mailto:nicolaisen@mci.sdu.dk)

† [ct@mci.sdu.dk](mailto:ct@mci.sdu.dk)

to fully equip the reader to use the methods themselves.

## II. OPTICAL CONDUCTIVITY OF SINGLE-LAYER 2D MATERIALS

The optical properties of a single-layer 2D material can be contained in the angular frequency  $\omega$ -dependent optical conductivity  $\sigma(\omega)$  at an infinitely thin interface. This method allows the 2D material to be introduced in any EM description through boundary conditions. Throughout this paper, we consider some interface at  $\mathbf{r}_0$  between two media of electric and magnetic fields  $\mathbf{E}_1, \mathbf{H}_1$  and  $\mathbf{E}_2, \mathbf{H}_2$  with the unit vector  $\hat{\mathbf{n}}$  normal to the interface. In the absence of surface currents, we have continuity of both the tangential electric and magnetic field across the interface. But if a 2D layer is placed along the interface, an optical surface conductivity is introduced, resulting in the tangential electric field  $\mathbf{E}_\parallel$  at the interface  $\mathcal{S}$  inducing a surface current given by Ohm's law as  $\mathbf{K} = \sigma(\omega)\mathbf{E}_\parallel|_{\mathcal{S}}$ . This causes a discontinuity of the tangential magnetic field components across the interface, giving conductive boundary conditions

$$\hat{\mathbf{n}} \times (\mathbf{E}_2 - \mathbf{E}_1)|_{\mathcal{S}} = \mathbf{0}, \quad (1)$$

$$\hat{\mathbf{n}} \times (\mathbf{H}_2 - \mathbf{H}_1)|_{\mathcal{S}} = \mathbf{K}. \quad (2)$$

These boundary conditions lead to a set of four linear equations that connect the two media with four unknowns as the electric and magnetic field amplitudes for two orthogonal polarizations each. A known optical conductivity of the 2D material  $\sigma(\omega)$  is required in order to solve these equations for the EM fields of the system.

### A. Optical conductivity of hBN obtained from first-principle calculations

hBN is an insulating material, where boron and nitrogen atoms are arranged in a hexagonal crystal structure similar to graphene. In the infrared (IR), hBN exhibits phonon polaritons [19], but more interesting for this work is that hBN has shown strong excitonic resonances in the ultraviolet (UV) [25, 26]. Ferreira et. al. [27] have determined the exciton energies from first-principles as  $\hbar\omega_1 = 5.48$  eV and  $\hbar\omega_2 = 6.41$  eV for hBN in the UV range. Inserting these exciton energies into the Elliot equation [28], we obtain the optical conductivity of single-layer hBN as

$$\frac{\sigma^{\text{hBN}}(\omega)}{\sigma_0} = 4i\hbar\omega \sum_{n=1}^2 \frac{p_n}{\hbar\omega - \hbar\omega_n + i\hbar\gamma_E}, \quad (3)$$

where  $\sigma_0 = e^2/4\hbar$  with  $e > 0$  being the elementary charge and  $\hbar$  the reduced Planck constant. The summation is over the excitonic states  $n = \{1, 2\}$ . Exciton relaxation processes have been investigated [29] for the 2D semiconductors WS<sub>2</sub> and MoSe<sub>2</sub>, where the temperature-dependent linewidth is shown to take values in the range

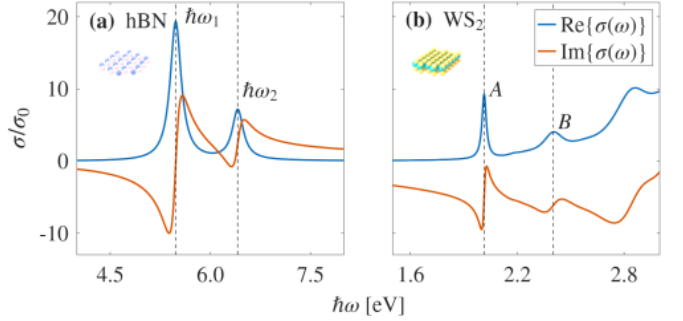


FIG. 1. Optical conductivity of monolayer (a) hBN, obtained as discussed in Sec. II A, and (b) WS<sub>2</sub>, obtained as discussed in Sec. II B. Both optical conductivities are normalized to  $\sigma_0 = e^2/4\hbar$  and given in terms of the real (imaginary) part as the blue (red) curve. The vertical dashed lines denote the main excitons in the two materials.

of tens of meV. For the sake of keeping the implementation of the optical conductivity simple, we assume that a similar linewidth is applicable for hBN and we therefore use a value  $\hbar\gamma_E = 0.1$  eV in the Elliott equation. The parameters  $p_1 = 0.088$  and  $p_2 = 0.027$  correspond to the weight of each exciton energy as they are implemented in the Elliott equation. Fig. 1a shows the real (imaginary) component of the optical conductivity given by the Elliott equation for hBN as the blue (red) curve in an energy window from  $\hbar\omega = 4$  eV to 8 eV. The exciton energies  $\hbar\omega_1$  and  $\hbar\omega_2$  are shown as vertical dashed lines. When excited by radiation matching these energies, the excitons carry charge across the atomically thin surface, leading to the non-zero optical conductivity.

### B. Optical conductivity of WS<sub>2</sub> obtained from experimental data

TMDs are a class of 2D semiconductors consisting of a layer of transition metal atoms between two layers of chalcogen atoms, with the layers bonded by van der Waals forces. To better connect with experimental activities, instead of resorting to first-principles calculations, we describe here WS<sub>2</sub> directly through experimental data. The optical conductivities of four different TMDs have been determined in Ref. [30] from their experimentally measured reflectance spectra. We focus on WS<sub>2</sub> as a material with a strong excitonic response in the visible regime. The single layer of WS<sub>2</sub> is treated as a homogeneous medium with an effective thickness given as the interlayer spacing,  $d = 0.618$  nm, of bulk WS<sub>2</sub>. The relative permittivity is modeled as a linear combination of  $N = 9$  Lorentzian oscillators

$$\varepsilon^{\text{WS}_2}(\omega) = \varepsilon_\infty + \sum_{k=1}^N \frac{f_k}{\hbar^2\omega_k^2 - \hbar^2\omega^2 - i\hbar^2\omega\gamma_k}, \quad (4)$$

with  $\hbar\omega_k$  being the resonance energy of each of the nine Lorentzian oscillators. The oscillator strength  $f_k$  and

linewidth  $\gamma_k$  of each oscillator are fitted to the experimental data in the energy window from  $\hbar\omega = 1.5$  eV to 3.0 eV, with the fitting parameters for WS<sub>2</sub> given in the supplementary material of Ref. [30]. While a value of  $\varepsilon_\infty$  for use in Eq. (4) is not given in the reference, here it has been chosen as  $\varepsilon_\infty = 10.68$  in order to align the value at the first local maximum of the real part of the optical conductivity to the curve given by Ref. [31]. The material response is now given as an optical sheet conductivity

$$\sigma^{\text{WS}_2}(\omega) = -i\varepsilon_0\omega[\varepsilon^{\text{WS}_2}(\omega) - 1]d, \quad (5)$$

where the real and imaginary part are both shown in Fig. 1b normalized to  $\sigma_0 = e^2/4\hbar$ . The two lowest-energy peaks marked by vertical dashed lines in the optical conductivity spectrum correspond to the excitonic features associated with interband transitions at the  $K$  ( $K'$ ) points of the Brillouin zone, where WS<sub>2</sub> shows valence band maxima and conduction band minima, and where spin-orbit coupling causes a splitting of the valence band, leading to two distinct peaks [32]. These peaks are denoted as the  $A$  and  $B$  lines of WS<sub>2</sub>. The broader response at higher energies is attributed to additional interband transitions.

### III. EXCITONS IN PERIODIC RIBBONS OF 2D MATERIALS

In this section, we consider an array of ribbons along a planar interface as a well-established geometry for investigating the scattering of light using 2D materials. We focus on two tested methods [33, 34] to analytically model such ribbons; an edge condition method and a Fourier series approach. For both methods, the optical properties of the single-layer 2D material are included as an optical conductivity. We consider a transverse magnetic (TM)-polarized wave of wave vector  $\mathbf{k}_1 = k_x\hat{\mathbf{x}} + k_z\hat{\mathbf{z}}$  in the  $xz$  plane, initially in a medium  $\varepsilon_1$  impinging at an angle  $\theta$  onto a substrate  $\varepsilon_2$ , with the interface along  $z = 0$  as shown in Fig. 2. This interface  $z = 0$  is patterned with ribbons of width  $w$  of the 2D material to form a one-dimensional grating with a periodicity  $L = 2w$  along  $x$ . For this TM polarization, the EM fields incident on this grating are given as

$$\mathbf{B}^i(\mathbf{r}, t) = \hat{\mathbf{y}}B_0^i e^{i(\mathbf{k}_1 \cdot \mathbf{r} - \omega t)}, \quad (6)$$

$$\mathbf{E}^i(\mathbf{r}, t) = (\hat{\mathbf{x}}E_{0x}^i + \hat{\mathbf{z}}E_{0z}^i)e^{i(\mathbf{k}_1 \cdot \mathbf{r} - \omega t)}. \quad (7)$$

Due to the periodicity of the 2D material, the EM fields reflected by the grating are given by the Fourier-Floquet decomposition

$$\mathbf{B}^r(\mathbf{r}) = \hat{\mathbf{y}} \sum_{n=-\infty}^{\infty} r_n e^{i(q_n x - \kappa_{1,n} z)}, \quad (8)$$

$$\mathbf{E}^r(\mathbf{r}) = -\frac{c^2}{\omega\varepsilon_1} \sum_{n=-\infty}^{\infty} r_n (\hat{\mathbf{x}}\kappa_{1,n} + \hat{\mathbf{z}}q_n) e^{i(q_n x - \kappa_{1,n} z)}, \quad (9)$$

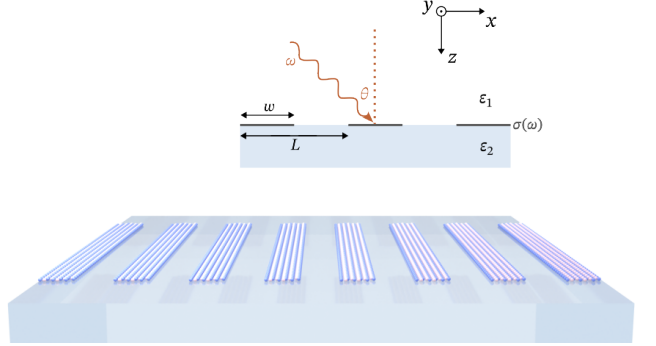


FIG. 2. Schematic (upper) and illustration (lower) of the system described in Sec. III consisting of nanoribbons of a 2D semiconductor of optical conductivity  $\sigma(\omega)$  that are infinitely long in the  $y$  direction, with a finite width  $w$  and a periodicity  $L$  along  $x$ . The interface of nanoribbons is placed between dielectrics  $\varepsilon_1$  and  $\varepsilon_2$ , and it is illuminated by plane waves of angular frequency  $\omega$  incident at an angle  $\theta$  onto the interface.

for the speed of light in vacuum  $c$ , and the transmitted EM fields propagating in the substrate  $\varepsilon_2$  are likewise given by

$$\mathbf{B}^t(\mathbf{r}) = \hat{\mathbf{y}} \sum_{n=-\infty}^{\infty} t_n e^{i(q_n x - \kappa_{2,n} z)}, \quad (10)$$

$$\mathbf{E}^t(\mathbf{r}) = \frac{c^2}{\omega\varepsilon_2} \sum_{n=-\infty}^{\infty} t_n (\hat{\mathbf{x}}\kappa_{2,n} - \hat{\mathbf{z}}q_n) e^{i(q_n x + \kappa_{2,n} z)}. \quad (11)$$

These decompositions are given in terms of Bloch modes of the transverse wave vector component

$$q_n = k_x + nG, \quad (12)$$

with the reciprocal lattice constant  $G = 2\pi/L$  of the nanoribbons. For the total wave number  $\sqrt{\varepsilon_i}k_0$ , where  $k_0 = \omega/c$  is the free-space wave number, in the medium with permittivity  $\varepsilon_i$ , the normal wave vector component  $\kappa_{i,n}$  in each medium is given by the equation

$$q_n^2 + \kappa_{i,n}^2 = \varepsilon_i k_0^2. \quad (13)$$

The coefficients  $r_n$  and  $t_n$  associated with the  $n$ 'th Bloch mode are reflection and transmission coefficients, which we will need to obtain the reflectance, transmittance, and absorbance of the nanoribbon. Not all Bloch modes  $n$  are propagating modes, in fact most exist only in the near field, and only reflection and transmission coefficients corresponding to propagating Bloch modes contribute to the reflectance, transmittance, and absorbance. At the interface  $z = 0$ , the transmitted electric field component along  $x$  produces a current along the nanoribbons, which is described by an optical conductivity  $\sigma(x)$  that depends on position  $x$  along the grating. Within a unit cell of length  $L$ , this position-dependent optical conductivity can be written as

$$\sigma(x) = \sigma(\omega)\Theta(w/2 - |x|), \quad (14)$$

where  $\Theta(x)$  is the Heaviside step function and  $\sigma(\omega)$  is the optical conductivity of a continuous layer of the 2D material.

### A. Edge condition method

Our starting point is to apply the edge condition method, where the main assumption is that the current perpendicular to the sharp edges of the hBN ribbon at  $x = \pm w/2$  is proportional to the distance to the edge, called the edge condition [35]. This assumption can be made when we consider radiation with small wavelengths compared to the width of the 2D semiconductor ribbons, written as  $kw < 1$ . We are able to obtain closed-form expressions for the reflectance, transmittance and absorbance at the cost of information about resonances of higher order than the fundamental dipole-like mode, which are not included in the ansatz. The edge condition gives the current within the 2D semiconductor ribbon at  $|x| \leq w/2$  as

$$\mathbf{K}(x) = \hat{\mathbf{x}}\chi e^{ik_xx} \sqrt{w^2/4 - x^2} \Theta(w/2 - |x|), \quad (15)$$

where  $\chi$  is a, for now, unknown coefficient. The surface current within  $|x| \leq w/2$  can also be written using Ohm's law as  $\mathbf{K}(x) = \sigma(x)\hat{\mathbf{x}} \cdot \mathbf{E}^t|_{z=0}\hat{\mathbf{x}}$ , where inserting Eq. (14) along with the Fourier-Floquet composition of the transmitted electric field of Eq. (9) leads to

$$\mathbf{K}(x) = \hat{\mathbf{x}} \frac{\sigma(\omega)c^2}{\omega\varepsilon_2} \Theta(w/2 - |x|) \sum_{n=-\infty}^{\infty} \kappa_{2,n} t_n e^{iq_n x}. \quad (16)$$

These two expressions for the surface current are set equal to one another, and both sides are multiplied by a basis function  $e^{-iq_n x}$  and integrated over the unit cell  $-L/2 \leq x \leq L/2$  to give the expression

$$\frac{\sigma(\omega)c^2}{\omega\varepsilon_2} \sum_{n=-\infty}^{\infty} \kappa_{2,n} t_n \frac{\sin[(m-n)\pi w/L]}{[(m-n)\pi w/L]} = \chi \frac{L}{4m} J_1\left(\frac{m\pi w}{L}\right), \quad (17)$$

where  $J_1(x)$  is the Bessel function of order 1. By inserting the Fourier-Floquet decompositions and the edge condition of Eq. (15) into the boundary conditions of Eqs. (1) and (2), multiplying each side of both boundary conditions with a basis function  $e^{-iq_n x}$  and integrating over the unit cell yields, after some algebra and in combination with Eq. (17), the reflection and transmission coefficients of the nanoribbons as

$$\frac{t_m}{B_0^i} = \frac{\varepsilon_2 \kappa_{1,m}}{\varepsilon_1 \kappa_{2,m} + \varepsilon_2 \kappa_{1,m}} \left[ 2\delta_{m0} - \mu_0 \frac{\chi}{B_0^i} \frac{w}{4m} J_1(m\pi w/L) \right], \quad (18)$$

and then

$$\frac{r_m}{B_0^i} = \frac{k_z}{\kappa_{1,m}} \delta_{m0} - \frac{\varepsilon_1}{\varepsilon_2} \frac{\kappa_{2,m}}{\kappa_{1,m}} \frac{t_m}{B_0^i}, \quad (19)$$

and the coefficient  $\chi$  as

$$\frac{\chi}{B_0^i} = \frac{2\kappa_{2,0}\kappa_{1,0}}{\varepsilon_1\kappa_{2,0} + \varepsilon_2\kappa_{1,0}} \frac{\sigma(\omega)c^2}{\omega} \frac{1}{\Lambda(\omega)}, \quad (20)$$

for a frequency-dependent factor with dimensions of length

$$\Lambda(\omega) = \sum_{n=-\infty}^{\infty} \frac{w}{4n} J_1\left(\frac{n\pi w}{L}\right) \left[ 1 + \frac{\sigma(\omega)}{\omega\varepsilon_0} \frac{\kappa_{2,n}\kappa_{1,n}}{\varepsilon_1\kappa_{2,n} + \varepsilon_2\kappa_{1,n}} \right]. \quad (21)$$

This infinite sum in the expression for  $\Lambda(\omega)$  is computed for the  $n = 0$  term and for twice the  $n > 0$  terms, given that the summand is even with respect to  $n$ , up to a truncation  $n = N$ . For this study, a choice of  $N = 101$  leads to well-converged results for the coefficient  $\chi$ , where the choice of an odd integer  $N$  is required for a correct result. The convergence based on the choice of  $N$  is further discussed in Ref. [33].

In order to determine the transmittance, reflectance and absorbance, we need to consider the component of the Poynting vector along  $z$ , which is normal to the hBN interface. The time-averaged energy flux components along  $z$  for the incident, reflected and transmitted EM fields are given as

$$\langle S_z^i \rangle = \frac{c^2}{2\mu_0\omega} \text{Re} \left\{ \frac{k_z}{\varepsilon_1} \right\} |B_0^i|^2, \quad (22)$$

$$\langle S_{z,n}^r \rangle = -\frac{c^2}{2\mu_0\omega} \text{Re} \left\{ \frac{\kappa_{1,n}}{\varepsilon_1} \right\} |r_n|^2, \quad (23)$$

$$\langle S_{z,n}^t \rangle = \frac{c^2}{2\mu_0\omega} \text{Re} \left\{ \frac{\kappa_{2,n}}{\varepsilon_2} \right\} |t_n|^2, \quad (24)$$

where  $\mu_0$  denotes the vacuum permeability. For the reflected and transmitted EM waves, we see that there exists a time-averaged energy flux component for each mode  $n$  present. The equation for the reflected wave shows that for a given mode  $n$ , any energy flux along  $z$  is only obtained if the wave number  $\kappa_{1,n} = \sqrt{\varepsilon_1 k_0^2 - q_n^2}$  remains real and represents a propagating wave, which is the case for  $\varepsilon_1 k_0^2 > q_n^2$ . If, on the other hand, we have  $\varepsilon_1 k_0^2 < q_n^2$ , then  $\kappa_{1,n} = i\sqrt{q_n^2 - \varepsilon_1 k_0^2}$  becomes imaginary and represents an evanescent wave that does not carry any energy along  $z$ . Similarly, for the transmitted wave, only modes  $n$  where  $\kappa_{2,n} = \sqrt{\varepsilon_2 k_0^2 - q_n^2}$  remains real and represents a propagating wave contribute to the energy flux. For the energy window of interest for hBN at  $\hbar\omega = 4$  eV to 8 eV, the condition  $kw < 1$  limits the ribbon widths to below around 25 nm. At normal incidence  $\theta = 0$  and for a periodicity given as twice the ribbon width  $L = 2w$ , the relative permittivities in the surrounding dielectrics would need to satisfy the condition

$$\varepsilon_j > \frac{\pi^2 c^2}{w^2 \omega^2} \quad (25)$$

in order to obtain propagating modes  $m = \pm 1$ . As a substrate, we consider a toy encapsulating dielectric of relative permittivity  $\varepsilon_1 = 3$  and a toy dielectric substrate

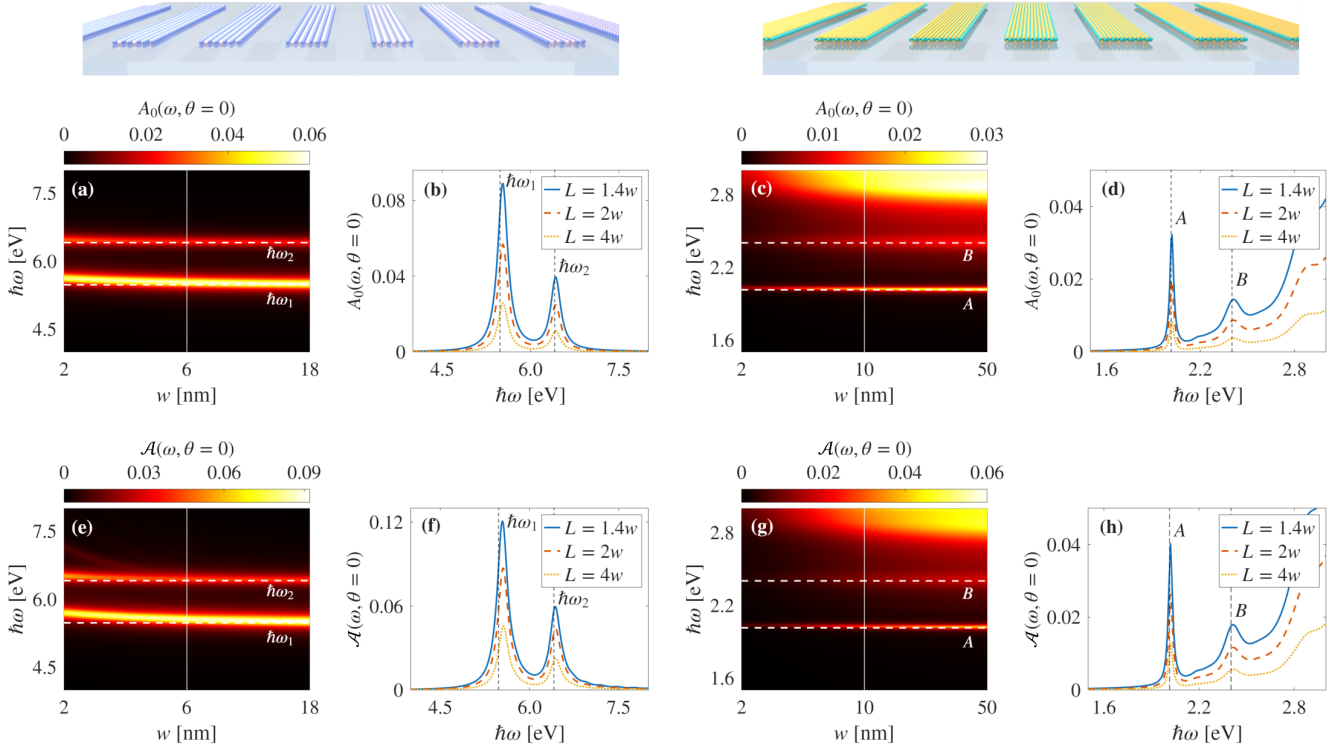


FIG. 3. Absorbance of nanoribbons of a 2D semiconductor encapsulated by a dielectric  $\varepsilon_1 = 3$  above, and a dielectric  $\varepsilon_2 = 4$  below, with radiation at normal incidence  $\theta = 0$ . (a) and (e) show contour maps of the absorbance for hBN nanoribbons computed using the edge condition method and the Fourier series method, respectively. The excitonic resonances of hBN are given as the horizontal dashed white lines, and the vertical solid white line marks a ribbon width of  $w = 6$  nm, where the absorbance of hBN nanoribbons at this width is given in (b) and (f) for three periodicities  $L$  of the nanoribbon arrays computed using the edge condition method and the Fourier series method, respectively. (c) and (g) show contour maps of the absorbance for WS<sub>2</sub> nanoribbons computed using the edge condition method and the Fourier series method, respectively. The  $A$  and  $B$  peaks of WS<sub>2</sub> are given as the horizontal dashed white lines and the vertical solid white line marks a ribbon width of  $w = 10$  nm, where the absorbance of WS<sub>2</sub> nanoribbons at this width is given in (d) and (h) for three periodicities  $L$  of the nanoribbon arrays computed using the edge condition method and the Fourier series method, respectively.

of a higher relative permittivity  $\varepsilon_2 = 4$ . For these dielectrics, the condition is not satisfied in the energy window of interest for hBN at ribbon widths below 25 nm in neither the substrate nor the surrounding dielectric, meaning that the  $n = 0$  mode remains the only propagating mode. Similarly, for the energy window of interest  $\hbar\omega = 1.5$  eV to 3 eV for WS<sub>2</sub> nanoribbons, the condition  $kw < 1$  leads to ribbon widths that are limited to below approximately 66 nm. For this width restriction, a periodicity  $L = 2w$ , and the relative permittivities  $\varepsilon_1 = 3$  and  $\varepsilon_2 = 4$ , the condition of Eq. (25) is again not satisfied at normal incidence in neither the substrate nor the surrounding dielectric. For a single propagating mode  $n = 0$ , all other modes  $n \neq 0$  are imaginary both above and below the 2D semiconductor. The reflectance, trans-

mittance, and absorbance are given as

$$R_0(\omega, \theta) = \left| \frac{r_0}{B_0^i} \right|^2, \quad (26)$$

$$T_0(\omega, \theta) = \frac{\text{Re}\{\varepsilon_1 \kappa_{2,0}\}}{\text{Re}\{\varepsilon_2 k_z\}} \left| \frac{t_0}{B_0^i} \right|^2, \quad (27)$$

$$A_0(\omega, \theta) = 1 - R_0(\omega, \theta) - T_0(\omega, \theta), \quad (28)$$

respectively. Given the linear relation between the transmission coefficient  $t_0$  and the incident magnetic field  $B_0^i$  from Eq. (18), the resulting reflectance becomes independent of the magnitude of the incident radiation. Similarly, the transmittance, and therefore also the absorbance, become independent of the magnitude of the incident radiation. The absorbance of hBN nanoribbons is shown in Fig. 3a across a range of ribbon widths  $w$  with a periodicity given as  $L = 2w$ . Around the excitonic resonances  $\hbar\omega_1$  and  $\hbar\omega_2$ , increases in absorbance are found across all ribbon widths, but as the ribbon width is decreased, the absorbance peaks slightly blueshift. Varying the periodicity  $L$  of the array at a constant ribbon width

of  $w = 6$  nm in Fig. 3b leads to variations in absorbance while the peaks are still at the excitonic resonances. The absorbance of WS<sub>2</sub> nanoribbons is similarly shown in Figs. 3c and 3d with peaks around the  $A$  and  $B$  lines and with a broad response at higher energies. Applying the edge condition method results in very poor tunability of the excitonic response by varying the width and periodicity of the ribbons. To further support this conclusion, we move on to study the same 2D semiconductor nanoribbons using a Fourier series method that doesn't use an ansatz for the form of the optical conductivity.

### B. Fourier series method

We now consider a method of writing the optical conductivity of the ribbons as a Fourier series, which requires solving a linear algebra problem. An important difference from the edge condition method is that, with no ansatz as to the form of the optical conductivity, we are no longer restricted by  $kw < 1$ . Furthermore, this method can be applied to any periodic modulation of the 2D material [36]. For TM polarization, the fields are again given as Fourier-Floquet series, which this time are given in a slightly different form

$$\mathcal{E}_x^{(j)}(x, z) = E_x^i e^{i(k_x x + k_z z)} \delta_{j1} + \sum_{n=-\infty}^{\infty} E_{x,n}^{(j)} e^{iq_n x - \xi_{j,n}|z|}, \quad (29)$$

$$\mathcal{E}_z^{(j)}(x, z) = E_z^i e^{i(k_x x + k_z z)} \delta_{j1} + \sum_{n=-\infty}^{\infty} E_{z,n}^{(j)} e^{iq_n x - \xi_{j,n}|z|}, \quad (30)$$

$$\mathcal{B}_y^{(j)}(x, z) = B_y^i e^{i(k_x x + k_z z)} \delta_{j1} + \sum_{n=-\infty}^{\infty} B_{y,n}^{(j)} e^{iq_n x - \xi_{j,n}|z|}, \quad (31)$$

where the index  $j = 1$  refers to the superstrate region  $z < 0$  with relative permittivity  $\varepsilon_1$ , and the index  $j = 2$  refers to the substrate region  $z > 0$  with relative permittivity  $\varepsilon_2$ . The incident wave number has components  $k_x = k_0 \sqrt{\varepsilon_1} \sin \theta$  and  $k_z = k_0 \sqrt{\varepsilon_1} \cos \theta$ , and the Bloch modes are again given as before. In this form of the Fourier-Floquet series, the wave numbers  $\xi_{j,n}$  are real and defined as  $\xi_{j,n} = \sqrt{q_n^2 - \varepsilon_j k_0^2}$  for evanescent waves  $q_n^2 < \varepsilon_j k_0^2$ . Conversely, the wave numbers are purely imaginary for propagating waves  $q_n^2 < \varepsilon_j k_0^2$ . The decomposition of the optical conductivity is in general given as

$$\sigma(x) = \sum_{m=-\infty}^{\infty} \tilde{\sigma}_m e^{imGx}, \quad (32)$$

where the coefficients are given as the integral

$$\tilde{\sigma}_m = \frac{1}{L} \int_L dx \sigma(x) e^{-imGx}. \quad (33)$$

Applying boundary conditions for this method yields a set of linear equations for all integers  $n$  that can be used

to determine the transmitted electric field Bloch components  $E_{x,n}^{(2)}$  along  $x$  for a given spatially dependent conductivity  $\sigma(x)$  of the hBN layer as

$$\left( \frac{\varepsilon_1}{\xi_{1,0}} + \frac{\varepsilon_2}{\xi_{2,0}} \right) E_{x,0}^{(2)} + \sum_{l=-\infty}^{\infty} \frac{i\tilde{\sigma}_{-l}}{\omega \varepsilon_0} E_{x,l}^{(2)} = \frac{2i\varepsilon_1}{k_z} E_x^i \quad \text{for } n = 0, \quad (34)$$

$$\left( \frac{\varepsilon_1}{\xi_{1,n}} + \frac{\varepsilon_2}{\xi_{2,n}} \right) E_{x,n}^{(2)} + \sum_{l=-\infty}^{\infty} \frac{i\tilde{\sigma}_{n-l}}{\omega \varepsilon_0} E_{x,l}^{(2)} = 0 \quad \text{for } n \neq 0. \quad (35)$$

The reflectance, transmittance, and absorbance for this methodology are given as

$$\mathcal{R}(\omega, \theta) = \sum_{n \in P} \frac{k_z}{|\xi_{1,n}|} |r_n|^2 \quad (36)$$

$$\mathcal{T}(\omega, \theta) = \sum_{n \in P} \frac{\varepsilon_2}{\varepsilon_1} \frac{k_z}{|\xi_{2,n}|} |t_n|^2, \quad (37)$$

$$\mathcal{A}(\omega, \theta) = 1 - \mathcal{R}(\omega, \theta) - \mathcal{T}(\omega, \theta), \quad (38)$$

respectively. These sums should only include the propagating modes,  $n \in P$ , where the wave numbers  $\xi_{i,n}$  are imaginary. It is sufficient to include the propagating modes, as the evanescent modes will not contribute to reflectance and transmittance in the far-field. The reflectivity coefficients are given as

$$r_n = \frac{E_{x,n}^{(2)}}{E_x^i} - \delta_{n0}, \quad (39)$$

and the transmittivity coefficients are given as

$$t_n = \frac{E_{x,n}^{(2)}}{E_x^i}. \quad (40)$$

The linear set of equations is applied to form 2D nanoribbons by modeling a unit cell of the modulated conductivity as Eq. (14). With this optical conductivity, the Fourier coefficients are given as

$$\tilde{\sigma}_0 = \frac{w}{L} \sigma(\omega) \quad \text{for } l = 0, \quad (41)$$

$$\tilde{\sigma}_l = \frac{1}{\pi l} \sigma(\omega) \sin \left( \frac{\pi l w}{L} \right) \quad \text{for } l \neq 0. \quad (42)$$

Because the rectangular wave is synthesized from an infinite sum of Fourier components, we now have an infinite set of Fourier coefficients for all integers  $l$ . Inserting these Fourier coefficients for the rectangular modulation into the linear equations of Eqs. (34) and (35), we obtain an infinite set of linear equations for all  $n$ , each with an infinite set of terms for all  $l$ , as

$$\cdots + \frac{i\sigma(\omega)}{\pi\omega\varepsilon_0} \sin\left(\frac{\pi w}{L}\right) E_{x,-1}^{(2)} + \left[ \frac{\varepsilon_1}{\xi_{1,0}} + \frac{\varepsilon_2}{\xi_{2,0}} + \frac{iw\sigma(\omega)}{\omega\varepsilon_0 L} \right] E_{x,0}^{(2)} + \frac{i\sigma(\omega)}{\pi\omega\varepsilon_0} \sin\left(\frac{\pi w}{L}\right) E_{x,1}^{(2)} + \cdots = 2i \frac{\varepsilon_1}{k_z} E_x^i \quad \text{for } n = 0, \quad (43)$$

$$\cdots + \frac{i\sigma(\omega)}{\pi\omega\varepsilon_0} \sin\left(\frac{\pi w}{L}\right) E_{x,n-1}^{(2)} + \left[ \frac{\varepsilon_1}{\xi_{1,n}} + \frac{\varepsilon_2}{\xi_{2,n}} + \frac{iw\sigma(\omega)}{\omega\varepsilon_0 L} \right] E_{x,n}^{(2)} + \frac{i\sigma(\omega)}{\pi\omega\varepsilon_0} \sin\left(\frac{\pi w}{L}\right) E_{x,n+1}^{(2)} + \cdots = 0 \quad \text{for } n \neq 0. \quad (44)$$

We now need to truncate both the number of equations  $n$  and the number of terms  $\ell$  in each equation. For simplicity, both  $n$  and  $\ell$  are chosen to be truncated as  $|n|, |\ell| > N$ . For this study, a choice of  $N = 100$  was implemented. This allows us to set up the set of linear equations as a matrix problem involving a  $(2N+1) \times (2N+1)$  matrix containing all the coefficients to the unknown fields  $E_{x,n}^{(2)}$ . This matrix problem is solved to determine the reflectance, transmittance, and absorbance using Eqs. (36) to (38) for the rectangular modulated layer of hBN.

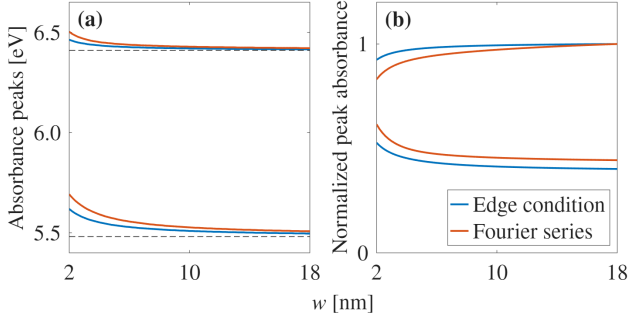


FIG. 4. Comparison of the edge condition and Fourier series method when applied to hBN nanoribbons of varying width  $w$  with a periodicity of  $L = 2w$  in an environment  $\varepsilon_1 = 3$  and substrate  $\varepsilon_2 = 4$  for radiation of normal incidence  $\theta = 0$ . (a) shows the spectral position of the two main peaks and (b) shows normalized peak values in absorbance for the edge condition (Fourier series) method as the blue (red) curves.

The absorbance of hBN nanoribbons obtained using the Fourier series method when varying the ribbon width is shown in Fig. 3e, where it is seen to align well with Fig. 3a obtained using the edge condition method. However, we do see a higher diffraction order of the upper mode for hBN in Fig. 3e as a very small peak that goes to higher energies when decreasing ribbon widths. As higher-order diffraction modes are not implemented into the ansatz of the current density in the edge condition method, this small peak is not present in Fig. 3a. The two main peaks of absorbance differ slightly in their spectral positions between the two methods at lower ribbon widths. For the system given in Figs. 3a and 3e, the spectral positions of the two peaks are plotted in Fig. 4a for hBN nanoribbons when using the edge condition (Fourier series) method as the two blue (red) curves. While both

methods capture the blueshift, the Fourier series method predicts a less significant shift.

In general, for both hBN and WS<sub>2</sub>, the Fourier series method predicts higher absorbance values for the two main peaks, as seen in Fig. 4b. The upper curve for each method corresponds to the lower-energy peak around the excitonic resonance  $\hbar\omega_1$  of hBN, as this peak shows a higher absorbance than the higher-energy peak around the excitonic resonance  $\hbar\omega_2$  of hBN. The blue (red) curves for the edge condition (Fourier series) method are normalized to the maximum absorbance obtained for the lower-energy peak at a ribbon width of  $w = 18$  nm. The Fourier series method illustrates how the edge condition method, while easy to implement, tends to underestimate the tunability of the response for 2D semiconductor ribbons. Unlike in graphene, where plasmons dominate the response, and these are very much geometry dependent, here we see how surface exciton polariton effects show little tunability with the dimensions of the ribbons, meaning that the coupling and hybridization of the excitons with an optical mode give very little freedom.

#### IV. LOCALIZED SURFACE EXCITONS IN SPHERICAL NPS

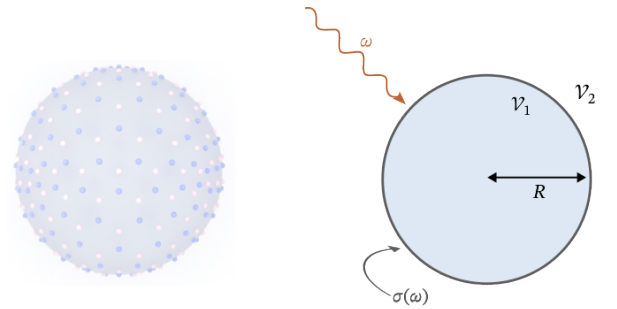


FIG. 5. Illustration (left) and schematic (right) of the system described in Sec. IV consisting of a spherical particle of radius  $R$  and a relative permittivity  $\varepsilon_1$  coated by a 2D material of conductivity  $\sigma(\omega)$ . The particle is placed in a medium of relative permittivity  $\varepsilon_2$  and is illuminated by a plane wave of angular frequency  $\omega$ .

We now consider the optical response of a spherical nanoparticle (NP) coated with a 2D semiconductor and

illuminated by a monochromatic plane wave, as illustrated in Fig. 5. The coupling of the external radiation with the excitons of the 2D semiconductor leads to localized exciton polaritons [37]. The formalism we apply to describe the response of spheres at the nanoscale was developed in 1908 by Gustav Mie [38]. Derivations for conventional particles in the absence of 2D materials can be found in textbooks [39, 40], and similar works including a conductive, 2D layer have been performed using graphene [41]. As the NP is illuminated, the charge carriers of the material, which are either free or bound depending on the nature of the material, are driven in oscillation by the electric field. The acceleration of these electric charges leads to EM energy radiating away from the particle, a mechanism known as scattering. However, through damping mechanisms such as collisions of the excitons, the motion of the charge carriers also leads to the transformation of the incident energy into other forms of non-radiative energy; a mechanism known as absorption. What follows is a description of Mie theory modified to include 2D materials at the surface of the particle.

### A. Modified Mie theory applied to 2D materials

The particle of radius  $R$  occupies a spherical region  $\mathcal{V}_1$  and is placed in a homogeneous host region  $\mathcal{V}_2$ , taken as a dielectric material of relative permittivity  $\varepsilon_2$ . Wave numbers in these regions are denoted as  $k_i = \sqrt{\varepsilon_i}k_0$  for  $i = 1, 2$ . We assume that the relative permeability of each material is given as  $\mu_i = 1$  for  $i = 1, 2$  in the optical regime. The analysis is limited to linear materials, and we work within the local response approximation (LRA), where a given material responds locally in space to the driving fields, meaning that the response functions of the material show no dependence on the wave vector  $\mathbf{k}$ ; they only, potentially, show dependence on the frequency  $\omega$  of incident radiation through nonlocality in time. Starting from Maxwell's equations and within LRA, the incident EM fields  $\mathbf{E}_{\text{inc}}, \mathbf{H}_{\text{inc}}$ , along with the fields inside the particle  $\mathbf{E}_1, \mathbf{H}_1$  and the fields scattered by the particle  $\mathbf{E}_{\text{sc}}, \mathbf{H}_{\text{sc}}$ , are expanded into spherical waves as solutions to the homogeneous, spherical Helmholtz equation. This leads to multipole expansions in the form

$$\mathbf{E}(\mathbf{r}) = \sum_{\ell=1}^{\infty} \sum_{m=-\ell}^{\ell} \left[ \frac{i}{k_i} a_{E\ell m} \nabla \times f_{\ell}(k_i r) \mathbf{X}_{\ell m}(\hat{\mathbf{r}}) + a_{H\ell m} f_{\ell}(k_i r) \mathbf{X}_{\ell m}(\hat{\mathbf{r}}) \right], \quad (45)$$

$$\mathbf{H}(\mathbf{r}) = \sqrt{\frac{\varepsilon_i \varepsilon_0}{\mu_i \mu_0}} \sum_{\ell=1}^{\infty} \sum_{m=-\ell}^{\ell} \left[ a_{E\ell m} f_{\ell}(k_i r) \mathbf{X}_{\ell m}(\hat{\mathbf{r}}) - \frac{i}{k_i} a_{H\ell m} \nabla \times f_{\ell}(k_i r) \mathbf{X}_{\ell m}(\hat{\mathbf{r}}) \right] \quad (46)$$

for unknown coefficients  $a_{P\ell m}$  where  $P = E, H$  and for functions  $f(k_i r)$  for  $i = 1, 2$ . These expansions are given in terms of vector spherical harmonics  $\mathbf{X}_{\ell m}(\hat{\mathbf{r}}) \equiv \hat{\mathbf{L}} Y_{\ell}^m(\hat{\mathbf{r}}) \delta_{0\ell} / \sqrt{\ell(\ell+1)}$  for Laplace's spherical harmonics  $Y_{\ell}^m(\hat{\mathbf{r}})$  of order  $\ell$  and  $m$  and an angular momentum operator  $\hat{\mathbf{L}} = -i(\mathbf{r} \times \nabla)$  [42]. Each term for a given value of  $\ell$  corresponds to the EM fields of a multipole, with  $\ell = 1$  being the electric and magnetic dipole contributions to the total fields,  $\ell = 2$  being quadrupole contributions, and so on. The vector spherical harmonics comply with orthonormality relations, a trait that is exploited once the boundary conditions are applied to the system. For the expansions of the incident EM fields, the unknown coefficients are denoted as  $a_{P\ell m}^0$ , and the functions  $f_{\ell}(x)$  are the spherical Bessel functions  $j_{\ell}(x)$  of order  $\ell$ . The incident plane wave is expanded in spherical waves in order to exploit the spherical symmetry of the problem, and they introduce spherical Bessel functions to the expansion of the incident EM fields. For the expansions of the EM fields inside the particle, the unknown coefficients are denoted as  $a_{P\ell m}^{\text{in}}$ , and the functions  $f_{\ell}(x)$  are again the spherical Bessel functions. While spherical Neumann functions  $y_{\ell}(x)$  of order  $\ell$  are also valid solutions to the homogeneous spherical Helmholtz equation,

they are not included in the functions  $f_{\ell}(x)$  for the internal EM fields, as they are diverging at  $r = 0$  and must be discarded as unphysical solutions. The asymptotic form of spherical Bessel functions of large arguments is appropriate to describe the localized exciton polaritons as standing spherical waves inside the particle [43].

For the expansions of the scattered EM fields, the unknown coefficients are denoted as  $a_{P\ell m}^+$ . In the region  $\mathcal{V}_2$ , both spherical Bessel functions and spherical Neumann functions are well-behaved, meaning that  $f_{\ell}(x)$  for the scattered-field expansions can be written in terms of spherical Hankel functions of the first kind  $h_{\ell}(x) = j_{\ell}(x) + iy_{\ell}(x)$  of order  $\ell$  as a linear combination of both linearly independent solutions to the spherical Helmholtz equation. The asymptotic form of spherical Hankel functions of large arguments are appropriate to describe propagating spherical waves outside the particle.

The total EM field outside the particle consists of both the incident fields and the scattered fields as  $\mathbf{E}_2 = \mathbf{E}_{\text{inc}} + \mathbf{E}_{\text{sc}}$  and  $\mathbf{H}_2 = \mathbf{H}_{\text{inc}} + \mathbf{H}_{\text{sc}}$ . In conventional Mie theory, the EM fields in the regions  $\mathcal{V}_1$  and  $\mathcal{V}_2$  are related by the continuity of the tangential field components at the particle interface  $r = R$ . However, as previously discussed, with a discontinuity of the tangential magnetic fields across the interface from the introduction of the 2D

coating, the scattering Mie coefficients, being the ratios

of unknown coefficients  $T_{P\ell} = a_{P\ell m}^+ / a_{P\ell m}^0$  for  $P = E, H$ , are given as

$$T_{E\ell} = \frac{j_\ell(x_1)\Psi'_\ell(x_2)\varepsilon_1 - \Psi'_\ell(x_1)j_\ell(x_2)\varepsilon_2 + g(\omega)\Psi'_\ell(x_1)\Psi'_\ell(x_2)}{\Psi'_\ell(x_1)h_\ell(x_2)\varepsilon_2 - j_\ell(x_1)\xi'_\ell(x_2)\varepsilon_1 - g(\omega)\Psi'_\ell(x_1)\xi'_\ell(x_2)}, \quad (47)$$

$$T_{H\ell} = \frac{j_\ell(x_1)\Psi'_\ell(x_2) - \Psi'_\ell(x_1)j_\ell(x_2) + g(\omega)x_0^2j_\ell(x_1)j_\ell(x_2)}{\Psi'_\ell(x_1)h_\ell(x_2) - j_\ell(x_1)\xi'_\ell(x_2) - g(\omega)x_0^2j_\ell(x_1)h_\ell(x_2)}. \quad (48)$$

Here, we have introduced dimensionless variables  $x_i = k_i R$  for  $i = 0, 1, 2$ , along with  $\Psi'_\ell(x)$  and  $\xi'_\ell(x)$  as the derivatives of the Riccati-Bessel functions  $\Psi_\ell(x) = xj_\ell(x)$  and  $\xi_\ell(x) = xh_\ell(x)$  with respect to their argument  $x$ . The surface conductivity due to the 2D coating is given by the dimensionless parameter

$$g(\omega) = \frac{i\sigma(\omega)}{\varepsilon_0\omega R}, \quad (49)$$

entering the third term of the numerator and denominator of both Mie coefficients. The conventional Mie coefficients are therefore restored by setting  $g(\omega) = 0$ . This is analogous to methods for including nonlocality in the NP description, where a surface response function, rather than a surface conductivity, appears in additional terms to both the numerator and the denominator of the conventional Mie coefficients [44, 45].

For NPs that are small compared to the wavelength of the incident radiation, at a given time any point within the particle experiences approximately the same phase of the incident EM fields, which is known as the quasistatic regime. This is compared to larger particles, where two points within the particle might be so separated as to experience the same field with a retardation between the two points. The quasistatic limit is given for radial points  $r$  such that  $k_i r \ll 1$  both inside and outside the particle,  $i = 1, 2$ , allowing for the spherical Bessel functions and spherical Hankel functions of the first kind to be written in their asymptotic forms [43] for arguments smaller than one as

$$j_n(z) \approx \frac{z^n}{(2n+1)!!}, \quad (50)$$

$$h_n^{(1)}(z) \approx -i \frac{(2n-1)!!}{z^{n+1}}. \quad (51)$$

Here, the double factorial notation  $(2n+1)!!$  and  $(2n-1)!!$  indicates the product of all odd positive integers up to  $2n+1$  and  $2n-1$ , respectively. With these asymptotic forms, the scattering Mie coefficients are approximately

$$T_{E\ell} \simeq \frac{i(\ell+1)x_2^{2\ell+1}}{(2\ell+1)!!(2\ell-1)!!} \frac{\varepsilon_1 - \varepsilon_2 + (\ell+1)g(\omega)}{(\ell+1)\varepsilon_2 + \ell\varepsilon_1 + \ell(\ell+1)g(\omega)}, \quad (52)$$

$$T_{H\ell} \simeq \frac{i(\ell+1)x_2^{2\ell+1}}{(2\ell+1)!!(2\ell-1)!!} \frac{(\ell+1)^{-1}x_0^2g(\omega)}{2\ell+1 - x_0^2g(\omega)}. \quad (53)$$

For a monochromatic plane wave flowing through a surface  $\mathcal{S}$  with unit vector  $\hat{\mathbf{n}}$  normal to the surface, the average power is

$$P = \int_S d^2\mathbf{r} \hat{\mathbf{n}} \cdot \langle \mathbf{S}(\mathbf{r}) \rangle, \quad (54)$$

where the Poynting vector averaged over a period of the wave is

$$\langle \mathbf{S}(\mathbf{r}) \rangle = \frac{1}{2} \text{Re}[\mathbf{E}(\mathbf{r}) \times \mathbf{H}^*(\mathbf{r})]. \quad (55)$$

The energy flow normal to the direction of propagation for the incident monochromatic plane wave of electric field amplitude  $\mathbf{E}_0$  is given as

$$\langle \mathbf{S}_0 \rangle \cdot \hat{\mathbf{k}} = \frac{1}{2} \sqrt{\frac{\varepsilon_2 \varepsilon_0}{\mu_2 \mu_0}} |\mathbf{E}_0|^2. \quad (56)$$

The scattered power is obtained by integrating the multipole expansions of the scattered field over a closed surface surrounding the particle, giving the expression

$$P_{\text{sc}} = \frac{\pi}{k_2^2} \sqrt{\frac{\varepsilon_2 \varepsilon_0}{\mu_2 \mu_0}} |\mathbf{E}_0|^2 \sum_{\ell=1}^{\infty} (2\ell+1)(|T_{E\ell}|^2 + |T_{H\ell}|^2). \quad (57)$$

The absorption power is, due to conservation of energy, the opposite of the total energy flow through the closed surface outside the particle. This observation yields the absorption power as  $P_{\text{abs}} = P_{\text{ext}} - P_{\text{sc}}$ , where the extinction power expresses the total energy provided by the incident wave to either scattering or absorption and is given as

$$P_{\text{ext}} = \frac{\pi}{k_2^2} \sqrt{\frac{\varepsilon_2 \varepsilon_0}{\mu_2 \mu_0}} |\mathbf{E}_0|^2 \sum_{\ell=1}^{\infty} (2\ell+1) \text{Re}(T_{E\ell} + T_{H\ell}). \quad (58)$$

The extinction is interpreted in experiments as the energy lost from the incident radiation when measuring the resulting radiation on the opposite side of the particle. The scattering cross section of the particle is the ratio of the power scattered by the particle relative to the incident energy flow normal to the direction of propagation [39]. The scattering cross section normalized to the geometric

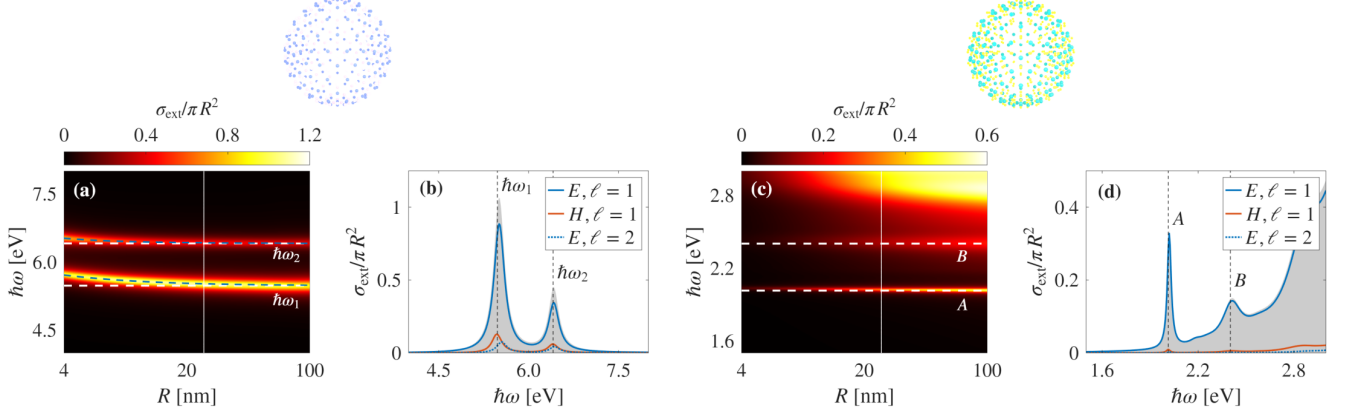


FIG. 6. Extinction cross section, normalized to the geometric cross section, of a hollow nanoshell of 2D semiconductors surrounded by air  $\varepsilon_1 = \varepsilon_2 = 1$ . (a) shows the extinction cross section of a hBN shell as a function of the radius  $R$ . The excitonic resonances  $\hbar\omega_1$  and  $\hbar\omega_2$  of monolayer hBN are shown as the horizontal white dashed lines, and the quasistatic electric dipole resonances of Eq. (61) are shown as the blue dashed curves. The vertical solid white line indicates a radius  $R = 25$  nm shown in panel (b). The electric dipole (quadrupole) contribution is shown as the solid (dashed) blue line, and the magnetic dipole contribution is shown as the solid red line, with the extinction cross section given as the shaded gray area. (c) shows the extinction cross section of a WS<sub>2</sub> shell as a function of the radius  $R$ . The  $A$  and  $B$  peaks are shown as the horizontal white dashed lines. The vertical solid white line indicates a radius  $R = 25$  nm shown in panel (d). Same as (b), showing the extinction cross section contributions of the WS<sub>2</sub> shell.

cross section  $\pi R^2$  of the particle is given in terms of the scattering Mie coefficients as

$$\sigma_{\text{sc}} = \frac{2}{(k_2 R)^2} \sum_{\ell=1}^{\infty} (2\ell + 1) (|T_{E\ell}|^2 + |T_{H\ell}|^2). \quad (59)$$

Similarly, the extinction cross section, normalized to the geometric cross section, is given in terms of the scattering Mie coefficients as

$$\sigma_{\text{ext}} = -\frac{2}{(k_2 R)^2} \sum_{\ell=1}^{\infty} (2\ell + 1) \text{Re}(T_{E\ell} + T_{H\ell}). \quad (60)$$

The absorption cross section, normalized to the geometric cross section  $\pi R^2$  of the particle, can be determined through the equation  $\sigma_{\text{abs}} = \sigma_{\text{ext}} - \sigma_{\text{sc}}$  by using values obtained by Eqs. (60) and (59).

## B. Hollow shells of hBN and WS<sub>2</sub>

Our starting point is a theoretical investigation of hollow shells, where the 2D semiconductor is placed in vacuum  $\varepsilon_1 = \varepsilon_2 = 1$ . This is the simplest possible example of implementing 2D materials into a spherical geometry, inspired from buckminsterfullerenes [46], and it is considered in order to investigate the behavior of the 2D material when patterned into spherical geometries. We first consider hollow hBN shells by applying the optical conductivity of Eq. (3) to the Mie coefficients of Eqs. (47) and (48) to determine the extinction cross section. A contour map of the extinction cross section is shown in Fig. 6a across a range of radii and energies. For each radius, we see two clear resonances, which are localized exciton polaritons for the hollow hBN shell. Each of the two

resonances are located near one of the monolayer exciton energies  $\hbar\omega_n$  for  $n = 1, 2$ , which are indicated by the vertical dashed lines. By considering the individual terms of  $T_{E\ell}$  and  $T_{H\ell}$  for any  $\ell$  in Eq. (60), we are able to identify each electric or magnetic multipole contribution to the total extinction cross section individually. As illustrated in Fig. 6b for a radius of  $R = 25$  nm, the extinction cross section, shown as the shaded gray area, mainly consists of an electric dipole contribution, given by the solid blue curve. Near the excitonic resonances of hBN, the driving fields cause collective oscillations of the excitons in the sphere with little to no retardation in order to form this electric dipole contribution. We also see a much less dominant magnetic dipole contribution, which appears due to the current introduced with the hBN layer at the surface of the particle. As the NP size is increased, the size of the current loop also increases, inducing a larger magnetic dipole. Due to retardation effects along the shell, we also see a small electric quadrupole contribution.

From a theoretical point of view, it is interesting to consider radii of the hollow hBN shell down to  $R = 4$  nm in the contour map, where both resonances start to shift to higher energies with a decreasing radius. In the limit of such small particles, an atomistic model of the particles would lead to more realistic results, but is beyond the scope of this article. The spectral positions of the extinction peaks for the hBN shell at low radii are predicted from the poles of the scattering Mie coefficients in the quasistatic limit. Given that the electric dipole is the dominating contribution to the extinction, we focus our attention on the poles of the electric scattering Mie coefficient for  $\ell = 1$ . For the hBN shell described by Eq. (3) in any dielectric environment, given by  $\varepsilon_1$  and  $\varepsilon_2$ , not restricted to vacuum, we obtain two electric dipole

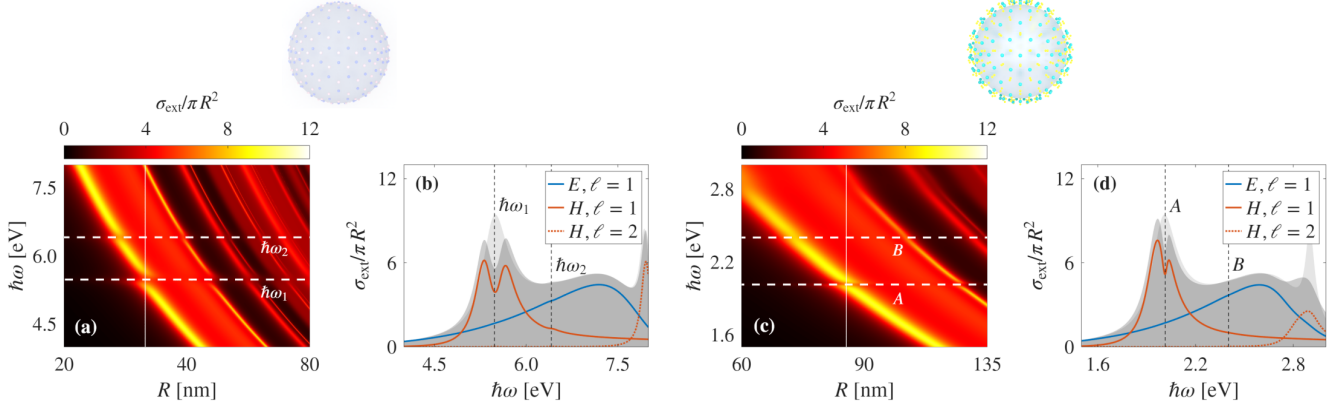


FIG. 7. Extinction cross section, normalized to the geometric cross section, of a dielectric core  $\varepsilon_1 = 11.7$  coated by a 2D semiconductor surrounded by air  $\varepsilon_2 = 1$ . (a) shows the extinction cross section of a hBN coating as a function of the radius  $R$ . The excitonic resonances  $\hbar\omega_1$  and  $\hbar\omega_2$  are shown as the horizontal white dashed lines. The solid vertical white line indicates a radius  $R = 31.6$  nm shown in panel (b). The electric dipole contribution is shown as the solid blue line, and the magnetic dipole (quadrupole) contribution is shown as the solid (dashed) red line, with the extinction cross section of the bare dielectric core given as the shaded light-gray area and the extinction cross section of the hBN coated particle given as the shaded dark-gray area. (c) shows the extinction cross section of a WS<sub>2</sub> coating as a function of the radius  $R$ . The  $A$  and  $B$  peaks are shown as the horizontal white dashed lines. The solid vertical white line indicates a radius  $R = 86.4$  nm shown in panel (d). Same as (b), showing the extinction cross section of the bare dielectric core and the contributions of the WS<sub>2</sub> coated dielectric particle.

resonances due to the two terms of the Elliot equation. These two electric dipole resonances are approximately given as

$$\omega_{\pm} \simeq \frac{1}{2}(\omega_1 + \omega_2) + \frac{\omega_E(p_1 + p_2)}{(2\varepsilon_2 + \varepsilon_1)} \pm \left[ \frac{1}{2} |\omega_1 - \omega_2| - \frac{\omega_E(p_1 - p_2)}{(2\varepsilon_2 + \varepsilon_1)} + \frac{\omega_E^2(p_1 + p_2)^2}{(2\varepsilon_2 + \varepsilon_1)^2 |\omega_1 - \omega_2|} \right]. \quad (61)$$

This equation positions the electric dipole resonances near the monolayer hBN excitonic resonances as  $\omega_- = \omega_1$  and  $\omega_+ = \omega_2$  but predicts a shift towards higher energies for a decreasing radius for both electric dipole resonances through the last two terms in the bracket. This approximation is shown in Fig. 6a as the dashed blue lines, showing excellent agreement with the full solution.

We now turn to hollow WS<sub>2</sub> shells by applying the optical conductivity of Eq. (5) to the Mie coefficients of Eqs. (47) and (48) to determine the extinction cross section. The resulting extinction cross section contour map is shown in Fig. 6c, where we see two resonance peaks around the  $A$  and  $B$  peaks, shown as the white dashed lines, along with a broader, higher-energy response. For a radius of  $R = 35$  nm, the extinction cross section of the hollow WS<sub>2</sub> shell is shown as the shaded gray area in Fig. 6d, where, as for the hollow hBN shell, we primarily see an electric-dipole contribution as the solid blue curve. This means that again, we see that the driving fields cause collective oscillations of the excitons in the sphere with little to no retardation. For decreasing radius, we see close to no shift towards higher energies of the two peaks as for hBN. Given the higher background

permittivity of WS<sub>2</sub> at  $\varepsilon_{\infty} = 10.68$ , as the radius of the NP decreases, the resonance frequency doesn't need to increase much for the function  $g(\omega)$  of Eq. (49) to remain at a value that leads to poles in Eq. (52) for  $\ell = 1$ . Above 2.5 eV, we again see a non-zero extinction cross section due to the external field interacting with the higher-lying interband transitions of WS<sub>2</sub>.

### C. Dielectric particles with conductive coating

As a means to a more realistic fabrication scenario, instead of a hollow shell, we now consider a toy dielectric core of  $\varepsilon_1 = 11.7$  with a coating of the 2D material, placed in vacuum ( $\varepsilon_2 = 1$ ). A dielectric core has no free charge carriers that respond to the external radiation. Instead, the external field causes polarization of the molecules that make up the dielectric, leading to local pairs of polarization charges. For large enough dielectric cores, retardation effects cause these polarization charges to oscillate out of phase, which induces a displacement current. Hence it is possible for a dielectric core to support both electric and magnetic multipoles. By introducing a conductive layer to the surface of the dielectric core, we allow for interaction between the excitons in the hBN layer and the polarization charges, causing a coupling of their oscillations and the formation of Mie-exciton polaritons [47, 48]. The extinction cross section for the dielectric particle with a hBN coating is seen in Fig. 7a, where the excitonic resonances of hBN are indicated by the dashed white lines. In the example of  $R = 31.6$  nm in Fig. 7b, we show the extinction cross section of the dielectric core with a hBN coating as the

dark-gray shaded area, compared to the extinction cross section of just the bare dielectric core as the light-gray shaded area. At this radius, a peak for the bare dielectric core aligns with the lower excitonic resonance of hBN, which causes a splitting of the extinction resonance for the hBN coated dielectric particle into two hybrid modes around the exciton resonances of hBN. This coupling is between the excitonic resonance of the hBN layer and the magnetic dipole of the dielectric, shown as the solid red line in Fig. 7b.

Turning to the same dielectric particle with a WS<sub>2</sub> coating, we see similar coupling between the dielectric and the *A* and *B* peaks of WS<sub>2</sub> for the extinction cross section in Fig. 7c. In Fig. 7d we focus on  $R = 86.4$  nm where we see the extinction cross section of the bare dielectric core aligns with the *A* peak of WS<sub>2</sub>, again allowing for coupling that causes a splitting of the peak [49]. At higher energies of around 2.8 eV, we also see that a peak in the bare dielectric core extinction cross section due to the magnetic quadrupole contribution is suppressed once the WS<sub>2</sub> coating is introduced. This is likely due to interactions of the dielectric with the excitons due to higher-lying interband transitions in WS<sub>2</sub>, which occur at these energies. Unlike in the 2D semiconductor nanoribbons, when turning to spherical particles, we both observe much more pronounced tunability with the geometry and hybridization with the core material.

## V. CONCLUSIONS

We have addressed different theoretical methods for determining the excitonic behavior of patterned 2D materials, focusing on hBN in the UV regime and on WS<sub>2</sub> in the visible, patterned into an array of ribbons or surrounding spherical particles. When considering periodic

ribbons of a 2D material, absorption peaks are observed for hBN ribbons near the intrinsic excitonic resonances of hBN, which are seen to shift to slightly higher energies for lower ribbon widths. Furthermore, by applying the Fourier series method, a higher diffraction order appears as a higher-energy absorption peak in the spectrum of hBN ribbons. Similarly, for WS<sub>2</sub>, absorption peaks appear very near the excitonic resonances (*A* and *B* peaks), exhibiting small shifts in energy for varying ribbon widths. For a spherical geometry, both hBN shells and WS<sub>2</sub> shells show extinction peaks very near the excitonic resonances of a planar sheet of hBN and the *A* and *B* peaks of WS<sub>2</sub>, respectively. When coating a dielectric or metallic core with a 2D material, we observe interactions of the excitons of the 2D material with the core, leading to splitting in the extinction resonances with the bare core. The spherical geometry therefore indicates a more fruitful path towards tunability and hybridization of the optical response in 2D semiconductors. This paper demonstrates the ease and versatility of applying the discussed methods, only requiring an optical conductivity for the 2D material in question to enable investigations of the optical response of the material. It should be noted that while this paper focuses on exciton polaritons contributing to the optical conductivities of materials, any polaritons leading to some contribution to the optical conductivity of a given material can be readily studied using the given methods.

## ACKNOWLEDGMENTS

We thank Joel D. Cox and Nuno M. R. Peres for discussions and proofreading the manuscript. The Center for Polariton-driven Light–Matter Interactions (POLIMA) is funded by the Danish National Research Foundation (Project No. DNRF165).

---

[1] K. S. Novoselov, A. K. Geim, S. V. Morozov, D. Jiang, Y. Zhang, S. V. Dubonos, I. V. Grigorieva, and A. A. Firsov, Electric field effect in atomically thin carbon films, *Science* **306**, 666 (2004).

[2] K. S. Novoselov, A. K. Geim, S. V. Morozov, D. Jiang, M. I. Katsnelson, I. V. Grigorieva, S. V. Dubonos, and A. A. Firsov, Two-dimensional gas of massless Dirac fermions in graphene, *Nature* **438**, 197 (2005).

[3] Y. Zhang, Y.-W. Tan, H. L. Stormer, and P. Kim, Experimental observation of the quantum Hall effect and Berry's phase in graphene, *Nature* **438**, 201 (2005).

[4] W. Zhang, Q. Wang, Y. Chen, Z. Wang, and A. T. S. Wee, Van der Waals stacked 2D layered materials for optoelectronics, *2D Mater.* **3**, 22001 (2016).

[5] Q. Zeng and Z. Liu, Novel optoelectronic devices: transition-metal-dichalcogenide-based 2D heterostructures, *Adv. Electron. Mater.* **4**, 1700335 (2018).

[6] J. Cheng, C. Wang, X. Zou, and L. Liao, Recent advances in optoelectronic devices based on 2D materials and their heterostructures, *Adv. Opt. Mater.* **7**, 1800441 (2019).

[7] D. N. Basov, A. Asenjo-Garcia, P. J. Schuck, X. Zhu, and A. Rubio, Polariton panorama, *Nanophotonics* **10**, 549 (2020).

[8] K. F. Mak, C. Lee, J. Hone, J. Shan, and T. F. Heinz, Atomically thin mos<sub>2</sub>: a new direct-gap semiconductor, *Phys. Rev. Lett.* **105**, 136805 (2010).

[9] Z. Y. Zhu, Y. C. Cheng, and U. Schwingenschlögl, Giant spin-orbit-induced spin splitting in two-dimensional transition-metal dichalcogenide semiconductors, *Phys. Rev. B* **84**, 153402 (2011).

[10] E. B. Nielsen and J. A. Schellman, The absorption spectra of simple amides and peptides, *J. Phys. Chem.* **71**, 2297 (1967).

[11] K. A. Bode and J. Applequist, Improved theoretical  $\pi$ - $\pi^*$  absorption and circular dichroic spectra of helical polypeptides using new polarizabilities of atoms and NC<sup>14</sup>O chromophores, *J. Phys. Chem.* **100**, 17825 (1996).

[12] K. P. Fears, D. Y. Petrovykh, S. J. Photiadis, and T. D. Clark, Circular dichroism analysis of cyclic  $\beta$ -helical peptides adsorbed on planar fused quartz, *Langmuir* **29**, 10095 (2013).

[13] A. Pospischil, M. M. Furchi, and T. Mueller, Solar-energy conversion and light emission in an atomic monolayer p–n diode, *Nat. Nanotech.* **9**, 257 (2014).

[14] B. W. H. Baugher, H. O. H. Churchill, Y. Yang, and P. Jarillo-Herrero, Optoelectronic devices based on electrically tunable p–n diodes in a monolayer dichalcogenide, *Nat. Nanotech.* **9**, 262 (2014).

[15] J. S. Ross, P. Klement, A. M. Jones, N. J. Ghimire, J. Yan, D. G. Mandrus, T. Taniguchi, K. Watanabe, K. Kitamura, and W. Yao, Electrically tunable excitonic light-emitting diodes based on monolayer WSe<sub>2</sub> p–n junctions, *Nat. Nanotech.* **9**, 268 (2014).

[16] C.-H. Lee, G.-H. Lee, A. M. van der Zande, W. Chen, Y. Li, M. Han, X. Cui, G. Arefe, C. Nuckolls, and T. F. Heinz, Atomically thin p–n junctions with van der Waals heterointerfaces, *Nat. Nanotech.* **9**, 676 (2014).

[17] S. Jo, N. Ubrig, H. Berger, A. B. Kuzmenko, and A. F. Morpurgo, Mono-and bilayer WS<sub>2</sub> light-emitting transistors, *Nano Lett.* **14**, 2019 (2014).

[18] O. Lopez-Sanchez, E. Alarcon Llado, V. Koman, A. Fontcuberta i Morral, A. Radenovic, and A. Kis, Light generation and harvesting in a van der Waals heterostructure, *ACS Nano* **8**, 3042 (2014).

[19] J. D. Caldwell, A. V. Kretinin, Y. Chen, V. Giannini, M. M. Fogler, Y. Francescato, C. T. Ellis, J. G. Tischler, C. R. Woods, and A. J. Giles, Sub-diffractive volume-confined polaritons in the natural hyperbolic material hexagonal boron nitride, *Nat. Commun.* **5**, 5221 (2014).

[20] N. Rivera, T. Christensen, and P. Narang, Phonon polaritonics in two-dimensional materials, *Nano Lett.* **19**, 2653 (2019).

[21] Z. Sun, J. Gu, A. Ghazaryan, Z. Shotan, C. R. Considine, M. Dollar, B. Chakraborty, X. Liu, P. Ghaemi, and S. Kéna-Cohen, Optical control of room-temperature valley polaritons, *Nat. Photon.* **11**, 491 (2017).

[22] B. Chakraborty, J. Gu, Z. Sun, M. Khatoniar, R. Bushati, A. L. Boehmke, R. Koots, and V. M. Menon, Control of strong light–matter interaction in monolayer ws<sub>2</sub> through electric field gating, *Nano Lett.* **18**, 6455 (2018).

[23] Y. Fan, Q. Wan, Q. Yao, X. Chen, Y. Guan, H. Alnatah, D. Vaz, J. Beaumariage, K. Watanabe, T. Taniguchi, J. Wu, Z. Sun, and D. Snoke, High efficiency of exciton-polariton lasing in a 2D multilayer structure, *ACS Photonics* **11**, 2722 (2024).

[24] D. N. Basov, A. Asenjo-Garcia, P. J. Schuck, X. Zhu, A. Rubio, A. Cavalleri, M. Delor, M. M. Fogler, and M. Liu, Polaritonic quantum matter, *Nanophotonics* **14**, 3723 (2025).

[25] K. Watanabe, T. Taniguchi, and H. Kanda, Direct-bandgap properties and evidence for ultraviolet lasing of hexagonal boron nitride single crystal, *Nat. Mater.* **3**, 404 (2004).

[26] B. Arnaud, S. Lebègue, P. Rabiller, and M. Alouani, Huge excitonic effects in layered hexagonal boron nitride, *Phys. Rev. Lett.* **96**, 026402 (2006).

[27] F. Ferreira, A. J. Chaves, N. M. R. Peres, and R. M. Ribeiro, Excitons in hexagonal boron nitride single-layer: a new platform for polaritonics in the ultraviolet, *J. Opt. Soc. Am. B* **36**, 674 (2019).

[28] A. J. Chaves, R. M. Ribeiro, T. Frederico, and N. M. R. Peres, Excitonic effects in the optical properties of 2D materials: an equation of motion approach, *2D Mater.* **4**, 025086 (2017).

[29] M. Selig, G. Berghäuser, A. Raja, P. Nagler, C. Schüller, T. F. Heinz, T. Korn, A. Chernikov, E. Malic, and A. Knorr, Excitonic linewidth and coherence lifetime in monolayer transition metal dichalcogenides, *Nat. Comm.* **7**, 13279 (2016).

[30] Y. Li, A. Chernikov, X. Zhang, A. Rigosi, H. M. Hill, A. M. van der Zande, D. A. Chenet, E.-M. Shih, J. Hone, and T. F. Heinz, Measurement of the optical dielectric function of monolayer transition-metal dichalcogenides: MoS<sub>2</sub>, MoSe<sub>2</sub>, WS<sub>2</sub>, and WSe<sub>2</sub>, *Phys. Rev. B* **90**, 205422 (2014).

[31] C. Hsu, R. Frisenda, R. Schmidt, A. Arora, S. M. de Vasconcellos, R. Bratschitsch, H. S. J. van der Zant, and A. Castellanos-Gomez, Thickness-dependent refractive index of 1L, 2L, and 3L MoS<sub>2</sub>, MoSe<sub>2</sub>, WS<sub>2</sub>, and WSe<sub>2</sub>, *Adv. Opt. Mat.* **7**, 1900239 (2019).

[32] C. Zhang, H. Wang, W. Chan, C. Manolatou, and F. Rana, Absorption of light by excitons and trions in monolayers of metal dichalcogenide MoS<sub>2</sub>: experiments and theory, *Phys. Rev. B* **89**, 205436 (2014).

[33] P. A. D. Gonçalves, E. J. C. Dias, Y. V. Bludov, and N. M. R. Peres, Modeling the excitation of graphene plasmons in periodic grids of graphene ribbons: An analytical approach, *Phys. Rev. B* **94**, 195421 (2016).

[34] P. A. D. Gonçalves and N. M. R. Peres, *An Introduction to Graphene Plasmonics* (World Scientific, 2016).

[35] K. Barkeshli and S. Khorasani, *Advanced Electromagnetics and Scattering Theory* (Springer, 2015).

[36] N. M. R. Peres, A. Ferreira, Y. V. Bludov, and M. I. Vasilevskiy, Light scattering by a medium with a spatially modulated optical conductivity: the case of graphene, *J. Phys.: Condens. Matter* **24**, 245303 (2012).

[37] M. J. Gentile, S. A. R. Horsley, and W. L. Barnes, Localized exciton–polariton modes in dye-doped nanospheres: a quantum approach, *J. Opt.* **18**, 015001 (2015).

[38] G. Mie, Beiträge zur Optik trüber Medien, speziell kolloidaler Metallösungen, *Ann. Phys.* **330**, 377 (1908).

[39] U. Hohenester, *Nano and Quantum Optics: An Introduction to Basic Principles and Theory* (Springer Nature, 2019).

[40] C. F. Bohren and D. R. Huffman, *Absorption and Scattering of Light by Small Particles* (John Wiley & Sons, 2008).

[41] T. Christensen, A.-P. Jauho, M. Wubs, and N. A. Mortensen, Localized plasmons in graphene-coated nanospheres, *Phys. Rev. B* **91**, 125414 (2015).

[42] J. D. Jackson, *Classical Electrodynamics*, 3rd ed. (Wiley, 1998).

[43] G. B. Arfken, H. J. Weber, and F. E. Harris, *Mathematical Methods for Physicists: A Comprehensive Guide* (Academic Press, 2011).

[44] I. J. Budiagaard, C. N. Hansen, P. E. Stamatopoulou, and C. Tserkezis, Quantum-informed plasmonics for strong coupling: the role of electron spill-out, *J. Opt. Soc. Am. B* **41**, 1144 (2024).

[45] N. Kyvelos, N. A. Mortensen, X. Zheng, and C. Tserkezis, Self-similar plasmonic nanolenses: mesoscopic ensemble averaging and chiral light–matter interactions, *J. Phys. Chem. C* **129**, 3635 (2025).

- [46] H. W. Kroto, J. R. Heath, S. C. O'Brien, R. F. Curl, and R. E. Smalley, C60: buckminsterfullerene, *Nature* **318**, 162 (1985).
- [47] F. Todisco, R. Malureanu, C. Wolff, P. A. D. Gonçalves, A. S. Roberts, N. A. Mortensen, and C. Tserkezis, Magnetic and electric mie-exciton polaritons in silicon nanodisks, *Nanophotonics* **9**, 803 (2020).
- [48] S. Wang, T. V. Raziman, S. Murai, G. W. Castellanos, P. Bai, A. M. Berghuis, R. H. Godiksen, A. G. Curto, and J. Gómez Rivas, Collective mie exciton-polaritons in an atomically thin semiconductor, *J. Phys. Chem. C* **124**, 19196 (2020).
- [49] C. Tserkezis, P. A. D. Gonçalves, C. Wolff, F. Todisco, K. Busch, and N. A. Mortensen, Mie excitons: Understanding strong coupling in dielectric nanoparticles, *Phys. Rev. B* **98**, 155439 (2018).